SDSS-IV MaNGA: environmental dependence of stellar age and metallicity gradients in nearby galaxies

Zheng Zheng,[1]★ Huiyuan Wang,[2] Junqiang Ge,[1] Shude Mao,[1,3,4] Cheng Li,[3,5] Ran Li,[1] Houjun Mo,[3,6] Daniel Goddard,[7] Kevin Bundy,[8] Hongyu Li,[1] Preethi Nair,[9] Lihwai Lin,[10] R. J. Long,[1,4] Rogério Riffel,[11,12] Daniel Thomas,[7] Karen Masters,[7] Dmitry Bizyaev,[13,14] Joel R. Brownstein,[15] Kai Zhang,[16] David R. Law,[17] Niv Drory,[18] Alexandre Roman Lopes[19] and Olena Malanushenko[13]

[1]*National Astronomical Observatories, Chinese Academy of Sciences, A20 Datun Road, Chaoyang District, Beijing 100012, China*
[2]*Key Laboratory for Research in Galaxies and Cosmology, Department of Astronomy, University of Science and Technology of China, Hefei, Anhui 230026, China*
[3]*Tsinghua Center for Astrophysics and Department of Physics, Tsinghua University, Beijing 100084, China*
[4]*Jodrell Bank Centre for Astrophysics, School of Physics and Astronomy, The University of Manchester, Oxford Road, Manchester M13 9PL, UK*
[5]*Shanghai Astronomical Observatory, Chinese Academy of Sciences, Shanghai 200030, China*
[6]*Department of Astronomy, University of Massachusetts Amherst, MA 01003, USA*
[7]*Institute of Cosmology and Gravitation, University of Portsmouth, Dennis Sciama Building, Burnaby Road, Portsmouth PO1 3FX, UK*
[8]*Kavli IPMU (WPI), UTIAS, The University of Tokyo, Kashiwa, Chiba 277-8583, Japan*
[9]*The University of Alabama, Tuscaloosa, AL 35487, USA*
[10]*Institute of Astronomy and Astrophysics, Academia Sinica, Taipei 10617, Taiwan*
[11]*Departamento de Astronomia, Instituto de Física, Universidade Federal do Rio Grande do Sul, CP 15051, 91501-970 Porto Alegre, RS, Brazil*
[12]*Laboratório Interinstitucional de e- Astronomia, Rua General José Cristino, 77 Vasco da Gama, Rio de Janeiro 20921-400, Brazil*
[13]*Apache Point Observatory and New Mexico State University, PO Box 59, Sunspot, NM 88349-0059, USA*
[14]*Sternberg Astronomical Institute, Moscow State University, Moscow 119991, Russia*
[15]*The University of Utah, Salt Lake City, UT 84112, USA*
[16]*University of Kentucky, Lexington, KY 40506, USA*
[17]*Space Telescope Science Institute, 3700 San Martin Drive, Baltimore, MD 21218, USA*
[18]*McDonald Observatory, The University of Texas at Austin, 1 University Station, Austin, TX 78712, USA*
[19]*Departamento de Física, Facultad de Ciencias, Universidad de La Serena, Cisternas 1200, La Serena, Chile*

ABSTRACT

We present a study on the stellar age and metallicity distributions for 1105 galaxies using the STARLIGHT software on MaNGA (Mapping Nearby Galaxies at APO) integral field spectra. We derive age and metallicity gradients by fitting straight lines to the radial profiles, and explore their correlations with total stellar mass M_*, $NUV - r$ colour and environments, as identified by both the large-scale structure (LSS) type and the local density. We find that the mean age and metallicity gradients are close to zero but slightly negative, which is consistent with the inside-out formation scenario. Within our sample, we find that both the age and metallicity gradients show weak or no correlation with either the LSS type or local density environment. In addition, we also study the environmental dependence of age and metallicity values at the effective radii. The age and metallicity values are highly correlated with M_* and $NUV - r$ and are also dependent on LSS type as well as local density. Low-mass galaxies tend to be younger and have lower metallicity in low-density environments while high-mass galaxies are less affected by environment.

Key words: galaxies: abundances – galaxies: evolution – galaxies: formation – galaxies: statistics – galaxies: stellar content – galaxies: structure.

★ E-mail: zz@bao.ac.cn

1 INTRODUCTION

Galaxies are complex systems and their structures are expected to be affected by many different processes. Observations have shown that the stellar age and metallicity gradients of galaxies are correlated with the overall properties of galaxies, such as total stellar mass, broad-band colour and stellar velocity dispersion (e.g. Mehlert et al. 2003; Koleva et al. 2009; Spolaor et al. 2009; Kuntschner et al. 2010; Rawle et al. 2010; La Barbera et al. 2012; González Delgado et al. 2015). Theoretically, internal processes such as supernova feedback (e.g. Kawata & Gibson 2003) and migration of stars (e.g. Sellwood & Binney 2002; Roškar et al. 2008) have been proposed to interpret the observed gradients. In the hierarchical galaxy formation scenario, galaxies are formed in dark matter haloes and could experience many mergers during their formation history. Galaxy properties could therefore be affected also by galaxy environments and merger history. Previous studies have also showed that galaxy properties related to mass and star formation history, e.g. total stellar mass (Kauffmann et al. 2004; Li et al. 2006), colour (Blanton et al. 2005; Li et al. 2006), D4000 (the break at 4000Å; Kauffmann et al. 2004; Li et al. 2006) and morphology (Dressler 1980), are strongly dependent on environment. Structure-related parameters, such as concentration, surface brightness and Sérsic indices, at given total stellar mass and colour, are however, nearly independent of the environment (Kauffmann et al. 2004; Blanton et al. 2005; Li et al. 2006; Blanton & Moustakas 2009).

There have been a lot of studies about relationships between galaxy properties and local density environment using various kinds of environment indicators, such as group environment (Yang et al. 2007), nearest-neighbour distance (Park et al. 2007) and number counts of neighbouring galaxies (Kauffmann et al. 2004; Blanton & Moustakas 2009). Most previous local density environment indicators are derived using galaxies, which may be a biased tracer of the underlying mass distribution. There have also been studies about the dependence of galaxy overall properties on large-scale structure (LSS) environments (e.g. Lee & Li 2008).

It is natural to ask whether the distribution of star formation history related parameters, such as stellar age and metallicity, depends on galaxy environments. On one hand, there are many numerical simulations studying the effects of mergers on stellar population distributions (e.g. Di Matteo et al. 2009; Pipino et al. 2010). Generally speaking, monolithic collapse models (Pipino et al. 2010) usually produce relatively large metallicity gradients, whilst mergers tend to make the profiles flatter (Di Matteo et al. 2009). However, secular evolution mechanisms such as stellar migrations (e.g. Roškar et al. 2008; Sánchez-Blázquez et al. 2009; Minchev et al. 2012) could also have large effects on stellar population distributions. On the other hand, there have been more and more resolved spectroscopic studies of stellar population distributions in galaxies (e.g. Yoachim, Roškar & Debattista 2010; Sánchez-Blázquez et al. 2014a,b; González Delgado et al. 2015; Morelli et al. 2015), but most of them have sample sizes of fewer than a few tens and none of them have explored the environmental dependence. Some photometric studies (e.g. Tortora et al. 2010; Tortora & Napolitano 2012; Zheng et al. 2015) and some spectroscopic studies using special techniques (Roig, Blanton & Yan 2015) have large samples but their results are affected either by the age–metallicity degeneracy or by poor spatial resolution.

Thanks to the Sloan Digital Sky Survey (SDSS) Mapping Nearby Galaxies at APO (MaNGA, Bundy et al. 2015) project, we are able to measure integrated field unit (IFU) spectra of 10 000 galaxies

and answer the question posed in the previous paragraph. Here in this paper, we use a method (Wang et al. 2009, 2012) based on reconstructed density field, instead of neighbouring galaxies, to derive the LSS environment information, and explore LSS environmental dependence of the stellar age and metallicity gradients. To do this, we use IFU spectra of more than 1000 galaxies from the 4th MaNGA Product Launch (MPL-4). In another two companion MaNGA papers by Goddard et al. (2016a,b), the dependence on galaxy properties and local density environment based on neighbour counts is considered.

The outline of the paper is as follows. We describe the data and galaxy sample in Section 2; we briefly introduce the methods for determining the LSS environment and stellar population parameters in Section 3; we then present our results in Section 4, and discuss the results in Section 5; and finally, we summarize our conclusions in Section 6.

2 DATA AND SAMPLE

MaNGA (Bundy et al. 2015; Yan et al. 2016b) is an IFU survey targeting about 10 000 nearby galaxies selected from the SDSS. The wavelength coverage is between 3600 and 10 300 Å with a spectral resolution $R \sim 2000$ (Drory et al. 2015). The sizes of the IFUs vary for different galaxies from 12 arcsec for a 19-fibre IFU to 32 arcsec for a 127-fibre IFU (Drory et al. 2015; Law et al. 2015). The MaNGA internal data release MPL-4 sample (equivalent to SDSS DR13 public release; Albareti et al. 2016) has a redshift range $0.01 < z < 0.15$ with a peak around $z = 0.03$. Fig. 1 shows the distributions of $NUV - r$ colour and $g - r$ colour versus the
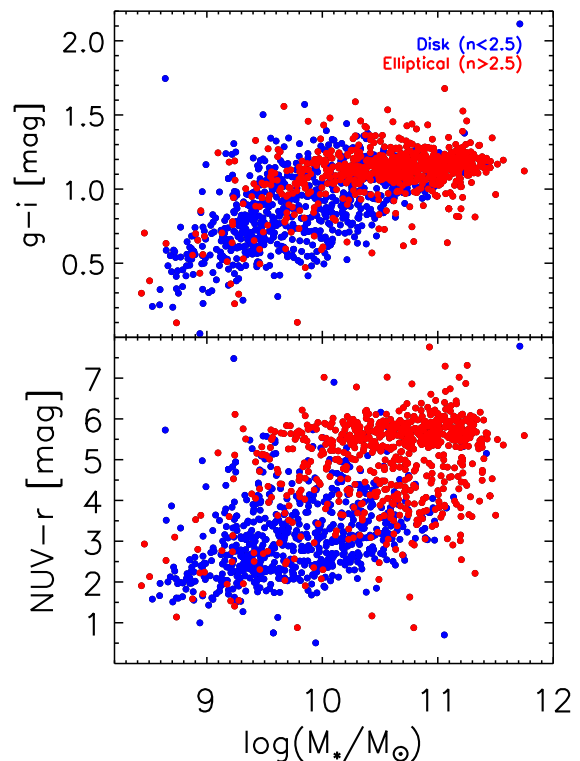

Figure 1. Mass–colour distribution of our sample. Red dots are for galaxies with Sérsic indices $n \geq 2.5$, which are more elliptical-like, so we call them 'elliptical' galaxies for short. Blue dots are for galaxies with $n < 2.5$, which are more disc-like, so we call them 'disc' galaxies for short. The NUV, SDSS g, r and i magnitudes, and total stellar mass M_* are from the NSA catalogue.
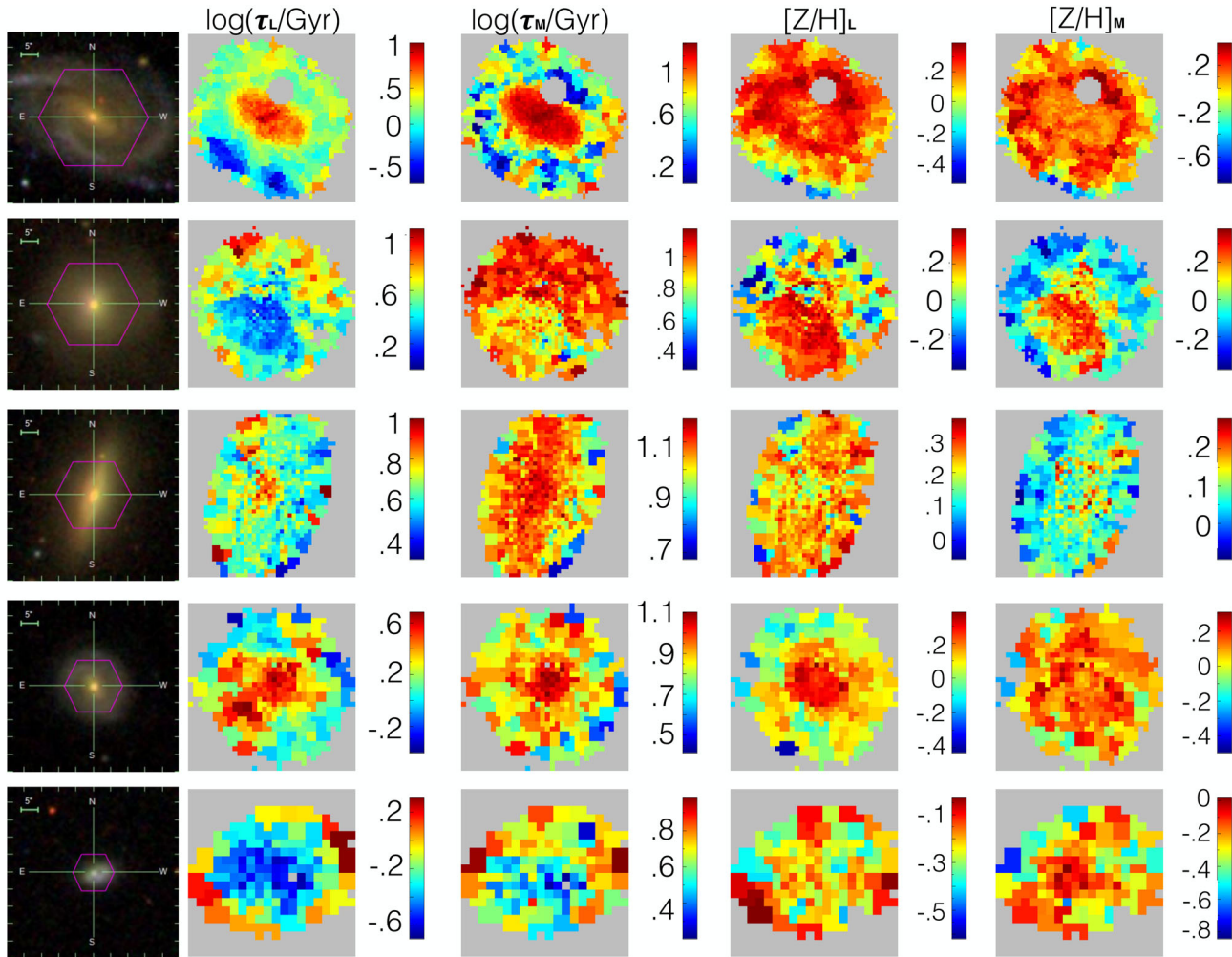
Figure 2. SDSS three-colour images and 2D maps of STARLIGHT derived parameters of five example galaxies. From left to right: SDSS three-colour image, luminosity-weighted age ($\log(\tau_L/\mathrm{Gyr})$) map, mass-weighted age ($\log(\tau_M/\mathrm{Gyr})$) map, luminosity-weighted metallicity ($[Z/H]_L$) map and mass-weighted metallicity ($[Z/H]_M$) map. The purple hexagons on the three-colour images show the fields of view of MaNGA observations. From top to bottom: a face-on spiral galaxy (MaNGA plate-IFU identifier: 8135-12701), an elliptical galaxy (8549-9101), an edge-on early-type galaxy (8612-6101), a face-on spiral galaxy with a bar (8549-3703) and an irregular galaxy (8549-1901). These five galaxies are observed using 127, 91, 61, 37 and 19 fibres (from top to bottom), respectively. Note that low signal-to-noise spaxels are removed from the 2D maps.

total stellar mass M_* of our sample galaxies. The M_*, $NUV - r$ colour, $g - r$ colour, redshift and n are obtained from the NASA Sloan Atlas[1] catalogue. The total stellar masses are derived from the fit to the SDSS five-band photometry with K-corrections (Blanton & Roweis 2007; Blanton et al. 2011) using the Bruzual & Charlot (2003) model and the Chabrier (2003) initial mass function (IMF). The Sérsic indices are derived using 2D Sérsic fits to the r-band SDSS images. A few example galaxies observed with different IFU bundle sizes are shown in Fig. 2. Detailed descriptions about the derivation of stellar population parameters shown in this figure can be found in Section 3.2.

The MaNGA sample is composed of primary sample, colour-enhanced sample and secondary sample. The main MaNGA sample galaxies are selected to lie within a redshift range, $z_{min} < z < z_{max}$, that depends on the absolute i-band magnitude (M_i) in the case of the primary and secondary samples, and on M_i and the $NUV - r$ colour in the case of the colour-enhanced sample. The values of

z_{min} and z_{max} are chosen so that both the number density of galaxies and the angular size distribution, matched to the IFU sizes, are roughly independent of M_i (or M_i and $NUV - r$ for the colour-enhanced sample). This results in lower and narrower redshift ranges for less luminous galaxies and higher and wider redshift ranges for more massive galaxies. At a given M_i (or M_i and $NUV - r$ colour for the colour-enhanced sample), the sample is effectively volume limited, so that all galaxies with $z_{min} < z < z_{max}$ are targeted independently of their other properties.[2] Two-thirds of the MaNGA sample (the primary sample + the colour-enhanced sample) are covered by IFU observations up to 1.5 effective radii (R_e) and the other third of the sample (the secondary sample) are covered up to 2.5 R_e. (Yan et al. 2016b, Wake et al., in preparation). Each target is observed using three dithers (Law et al. 2015) and the observed

[1] http://nsatlas.org

[2] This volume varies with M_i, and therefore a correction for this varying volume of selection is needed when calculating statistical values from the sample. We correct the galaxies back to a volume-limited sample by applying a weight (W) to each galaxy such that $W = V_r/V_s$, where V_r is an arbitrary reference volume.

data are reduced by the MaNGA data reduction pipeline (DRP; Law et al. 2016; Yan et al. 2016a). The current version of the DRP is 1_5_1 and the final products of the DRP are data cubes with a pixel size of 0.5 arcsec as well as row stacked spectra.

Our sample galaxies are taken from the MaNGA internal data release MPL-4 comprising 1351 unique galaxies. Of these, 1144 galaxies have large-scale environment information (see Section 3 for details). Furthermore, we remove 39 galaxies that either are too small for gradients to be derived or have multiple galaxies in the field of view. Our final sample contains 1105 galaxies, of which 538 have Sérsic indices $n < 2.5$ (disc-like) and 567 have $n \geq 2.5$ (elliptical-like). Note that the Sérsic index n is not an ideal indicator of galaxy morphology: some disc galaxies may have $n \geq 2.5$ while some elliptical galaxies may have $n < 2.5$. Broad-band colours, such as $NUV - r$ (e.g. Schiminovich et al. 2007), may help separate passive and star-forming galaxies, and we will analyse the impact of the $NUV - r$ colour in the following sections.

3 METHOD

We measure the density field around each MaNGA galaxy and classify its environment into one of four categories: cluster, filament, sheet or void. We measure its stellar age and metallicity at different parts of the galaxy using full spectral fitting method and then measure gradients and zero-points of the age and metallicity radial profiles. Finally, we compare the measured the gradients and zero-points of galaxies in different environments. We discuss each of these in turn.

3.1 Environment

In this paper, we consider two environment indicators: the local mass density and the type of LSS. The environment data are taken from the ELUCID project (Wang et al. 2016), which aims to perform constrained simulations of the local universe that can provide an optimal way to utilize and explain the abundant observational data. This project uses the halo-domain method developed by Wang et al. (2009) to reconstruct the cosmic density field in the local Universe from the SDSS DR7 galaxy group catalogue (Yang et al. 2007). As shown in Wang et al. (2016), the reconstructed density field matches well the distributions of both the galaxies and groups. The local mass density environment indicator of a galaxy is the density at the position of the galaxy smoothed by a Gaussian kernel with a smoothing scale of $1 \, \text{Mpc} \, h^{-1}$. Since the density field is reconstructed in real space, we have to correct for redshift distortions in the distribution of galaxies. The Kasier effect is corrected by using the method developed in Wang et al. (2012). To correct for the *Finger of God* effect, we first crossmatch our galaxy sample with the galaxy catalogue used to construct the group catalogue. We then use the group centre to represent the galaxy position in deriving the density field. We refer the reader to Wang et al. (2016) for the details of the reconstruction methods.

The morphology of the LSS is very complex. Recently, much effort has been given to developing methods to classify the cosmic web (e.g. Hahn et al. 2007; Hoffman et al. 2012). Here, we adopt a dynamical classification method developed by Hahn et al. (2007), which uses the eigenvalues of the tidal tensor to determine the type of the local structure in a cosmic web. The tidal tensor, $\mathcal{T}_{ij}$, is defined as

$$\mathcal{T}_{ij} = \partial_i \partial_j \phi, \tag{1}$$

where ϕ is the peculiar gravitational potential and can be calculated from the reconstructed density field shown above. Following Hahn et al. (2007), we smoothed the density field with a Gaussian kernel with a smoothing scale of $2 \, \text{Mpc} \, h^{-1}$. We then diagonalize the tidal field tensor T_{ij} and derive the eigenvalues T_1, T_2 and T_3, which corresponds to the major, intermediate and minor axes of the tidal field. The LSS environment is classified into four categories following the definition by Hahn et al. (2007): *cluster* has three positive eigenvalues ($T_1 > 0, T_2 > 0, T_3 > 0$, fixed points); *filament* has two positive and one negative eigenvalues ($T_1 > 0, T_2 > 0, T_3 < 0$, two-dimensional stable manifold); *sheet* has one positive and two negative eigenvalues ($T_1 > 0, T_2 < 0, T_3 < 0$, one-dimensional stable manifold); and *void* has three negative eigenvalues ($T_1 < 0, T_2 < 0, T_3 < 0$, unstable orbits). The method has been shown to very effectively classify the LSSs of local Universe (see Wang et al. 2016).

3.2 Stellar population analysis

We bin the MaNGA data cube of a galaxy using the Voronoi binning method (Cappellari & Copin 2003) so that each binned spectrum has a signal-to-noise ratio (SNR) equal to ~20 (determined in the 5800–6400Å wavelength range). Spaxels with SNR ≤ 5 or dominated by sky lines are removed before binning. We fit the Voronoi binned spectra using the STARLIGHT code (Cid Fernandes et al. 2005) using 150 bases from the model of Bruzual & Charlot (2003) with the STELIB stellar library (Le Borgne et al. 2003) and using a Chabrier (2003) IMF to obtain the stellar population parameters. The STARLIGHT bases are single stellar population templates defined using a grid of ages and metallicities. There are 25 ages (0.001, 0.003, 0.005, 0.007, 0.009, 0.01, 0.014, 0.025, 0.04, 0.055, 0.102, 0.161, 0.286, 0.509, 0.905, 1.278, 1.434, 2.5, 4.25, 6.25, 7.5, 10, 13, 15, 18 Gyr) and 6 metallicities (0.0001, 0.0004, 0.004, 0.008, 0.02, 0.05). We use the 3710–8000 Å part of the de-redshifted spectra in the STARLIGHT fitting because the parts of the spectrum outside this range are sometimes dominated by noise. Emission line regions are masked out using the STARLIGHT standard emission line mask file and other regions are weighted equally during the fitting. Note that in our companion papers by Goddard et al. (2016a,b), the FIREFLY software (Wilkinson et al. 2015) is used with the Maraston & Strömbäck (2011) model utilizing the MILES stellar library (Sánchez-Blázquez et al. 2006a) and a Kroupa (2001) IMF. In addition, they have a slightly different Voronoi binning scheme and their fitting wavelength range is 3600–6900 Å. (This different choice of wavelength range is owing to the wavelength restriction in their models.) Our results are in good agreement despite these differences.

The STARLIGHT code returns the best-fitting model, which is a mixture of different bases. Both the light fraction (determined around wavelength 4020 Å[3]) x and the current mass fraction M of each base are listed in the output file. We calculate the luminosity-weighted age using

$$\tau_L = \frac{\Sigma_j x_j \tau_j}{\Sigma_j x_j}, \tag{2}$$

---

[3] The choice of 4020 Å is the default setting of STARLIGHT. This wavelength range does not have emission lines and it has been proven to be a good choice by extensive tests.

where τ_j is the age value of the *j*th base and x_j is the light fraction of the *j*th base. Similarly, we calculate the luminosity-weighted metallicity using

$$Z_{\rm L} = \frac{\Sigma_j x_j Z_j}{\Sigma_j x_j}, \qquad (3)$$

where Z_j is the metallicity value of the *j*th base. We calculate the mass-weighted age and metallicity using

$$\tau_{\rm M} = \frac{\Sigma_j M_j \tau_j}{\Sigma_j M_j} \qquad (4)$$

and

$$Z_{\rm M} = \frac{\Sigma_j M_j Z_j}{\Sigma_j M_j}, \qquad (5)$$

where M_j is the current mass fraction of the *j*th base. Note that this is different from some earlier studies, e.g. González Delgado et al. (2015), who use $\log(\tau_j)$ and $\log(Z_j)$ before weighting. We use this definition because it is physically more intuitive. Also, the weighting formalism used by González Delgado et al. (2015) may give more weight to younger and metal poorer stellar populations.

After fitting the whole data cube, we create maps of the stellar population parameters, such as stellar age and metallicity. We radially bin these maps into elliptical annuli with widths of 0.1 effective radius ($R_{\rm e}$). Here $R_{\rm e}$ is defined as the major axis of the ellipse that contains 50 per cent of the total *r*-band flux of the galaxy. The effective radius, position angle and ellipticity of the galaxy are obtained by fitting Multi-Gaussian Expansion models (Cappellari et al. 2013) to the galaxy's *r*-band image. Finally, we derive the stellar population radial profiles using the median values of each annulus.

4 RESULTS

In this paper, we focus on the distributions of stellar age and metallicity because they are the two most important stellar population parameters. We use logarithmic values of age ($\log(\tau)$) and metallicity ([Z/H]) in the remainder of this paper. Five example galaxies observed with different IFU bundle sizes are shown in Fig. 2. We can see from these plots that distributions of stellar population parameters could roughly be fitted by concentric elliptical contours. Also, galaxy centres are generally older and more metal rich than the outer regions.

Bulges usually have a steep increase in age and metallicity towards the centre of a galaxy and they may have different formation histories from discs (Spiniello et al. 2015). We focus on the 'bulk' part of the galaxy, i.e. the more extended disc part. Therefore, we exclude bulges in studying the relationship between age and metallicity gradients and environments. According to Zheng et al. (2015), disc galaxies usually have bulge sizes about 0.3 r_{90} (r_{90} being the radius that contains 90 per cent of the total *r*-band flux) or 0.5 times the effective radius $R_{\rm e}$. Therefore, we measure the gradients between 0.5 $R_{\rm e}$ and 1.5 $R_{\rm e}$ because all MaNGA galaxies are fully covered by the IFUs up to 1.5 $R_{\rm e}$. We have examined the effect on our results if bulges are included and find that there is no significant change to our conclusions except that we would have larger scatters in the gradients. We fit the data points within our radial region with a straight line, defined as

$$\log(\tau(R/R_{\rm e})) = \log(\tau(0)) + k_\tau \, R/R_{\rm e}, \qquad (6)$$

for the stellar age profile, and

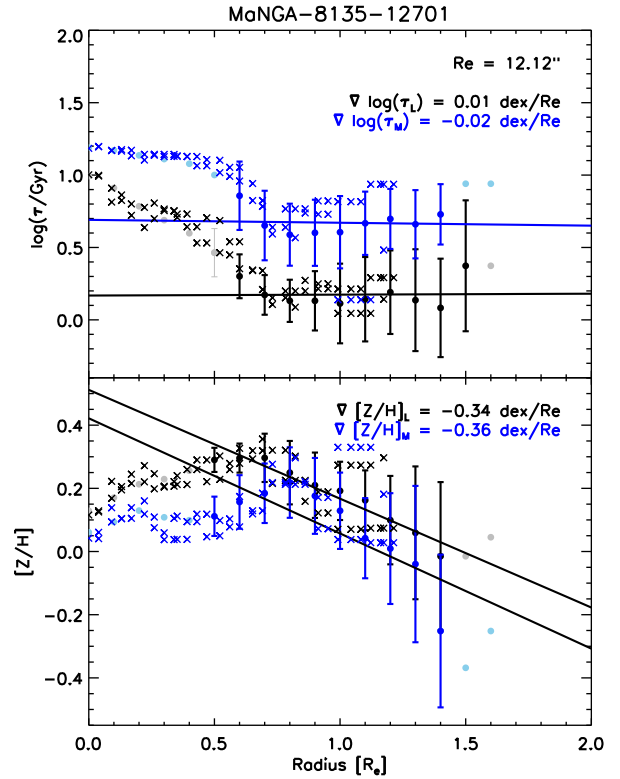$$[Z/H](R/R_{\rm e}) = [Z/H](0) + k_Z \, R/R_{\rm e}, \qquad (7)$$

Figure 3. A line fitting example for a MaNGA galaxy (the galaxy shown in the first row of Fig. 2). Upper panel: linear fitting of age profiles; lower panel: linear fitting of metallicity profiles. The dots show the median radial profiles and the lines show straight line fittings of the points within 0.5–1.5$R_{\rm e}$. The error bars show 1σ scatter within each radial bin. The crosses show values along the major axis of this galaxy. Black symbols are for luminosity-weighted values and blue symbols are for mass-weighted values.

for the stellar metallicity profile, where $R/R_{\rm e}$ is the radius in units of the effective radius $R_{\rm e}$, and k_τ and k_Z are age and metallicity gradients in units of dex/$R_{\rm e}$. Line fitting is performed using the robust linear regression method implemented in the IDL procedure ROBUST_LINEFIT, which can identify and remove bad data during the fitting. One example of the fitting is shown in Fig. 3. The gradient uncertainty is estimated using a Monte Carlo method, and is typically $\sim$0.1 dex/$R_{\rm e}$.

We present both the gradients and the fitted values at the effective radii, and explore their correlations with different galaxy properties and environments in the following sections.

4.1 Radial profiles

Before discussing the profile fitting results, we show the overall behaviour of the age and metallicity radial profiles by plotting the co-added radial profiles (Figs 4–7). We classify our galaxies using stellar mass M_* and Sérsic index *n*. We divide our sample into three mass bins: low mass ($\log(M_*/M_\odot) \leq 9.5$), intermediate mass ($9.5 < \log(M_*/M_\odot) \leq 10.5$) and high mass ($\log(M_*/M_\odot) > 10.5$). We further divide the galaxy sample into more disc-like ($n < 2.5$) and more elliptical-like ($n \geq 2.5$) galaxies. In each figure, we show the radial profiles for these different kinds of galaxies in black and the median value of these radial profiles in red dots. In order to guide the eye, we also plot the radial profiles
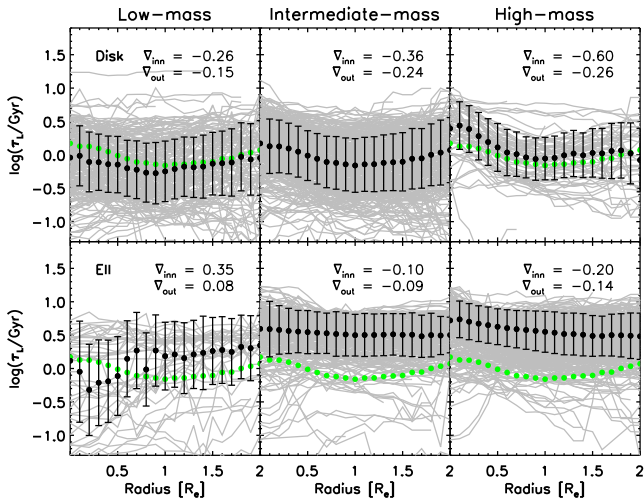
Figure 4. Co-added luminosity-weighted age profiles. The galaxies are split into six groups based on mass and morphology. Low mass (left-hand column) is $\log(M_*/M_\odot) \leq 9.5$, intermediate mass (middle column) is $9.5 < \log(M_*/M_\odot) \leq 10.5$, high mass (right-hand column) is $\log(M_*/M_\odot) > 10.5$; disc (top row) is $n < 2.5$ and elliptical (bottom row) is $n \geq 2.5$. The radial profiles are plotted with grey lines. The black dots with error bars show the median value and 1σ dispersion of the black lines; the green dots show the median value of intermediate-mass disc galaxies and are the same in all panels. Each panel also shows the gradient of the median profile in the inner region (within 0–$1\,R_e$) and in the outer region (within 0.5–$1.5\,R_e$).
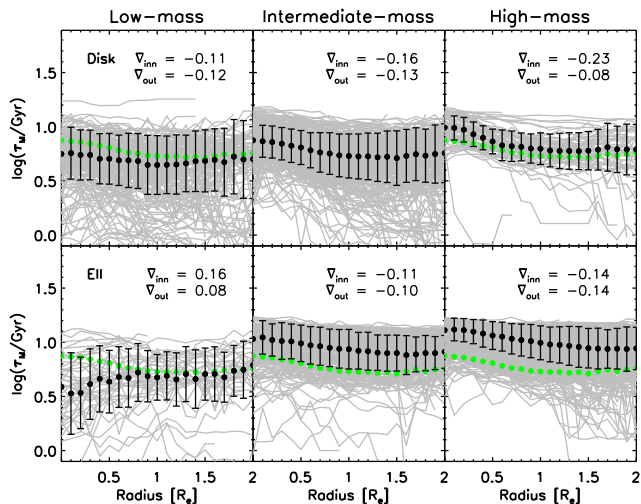
Figure 5. Co-added mass-weighted age profiles. The symbols are the same as in Fig. 4.

of intermediate-mass disc galaxies in grey and their median values in green dots in each panel.

In general, the mass-weighted age profiles are very flat. The luminosity-weighted age profiles are less flat and sometimes show a 'U' shape curve with the minimum value located around 1–$1.5\,R_e$. The median luminosity-weighted age profiles of the elliptical galaxies are about 0.1 dex older than those of the disc galaxies, and there is almost no dependence on M_*. The switch over in the low-mass elliptical panel (lower-left panel) of Fig. 4 may be due to small sample size. The individual galaxies with down-turn age profiles towards the centre of the galaxies might be caused by recent star formation (Ge et al., in preparation; Lin et al., in preparation)
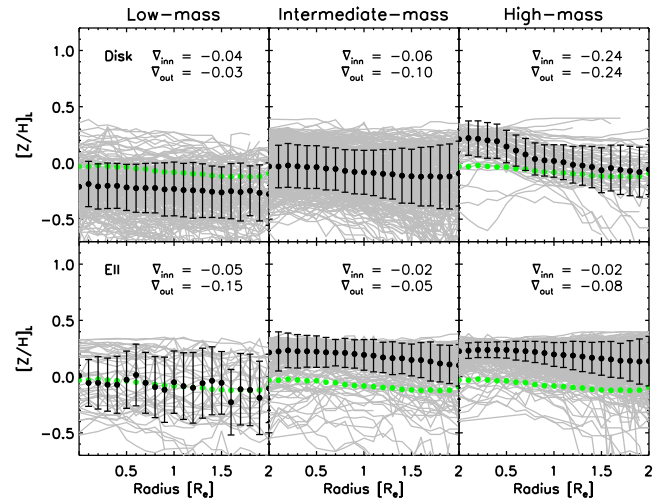
Figure 6. Co-added luminosity-weighted metallicity profiles. The symbols are the same as in Fig. 4.
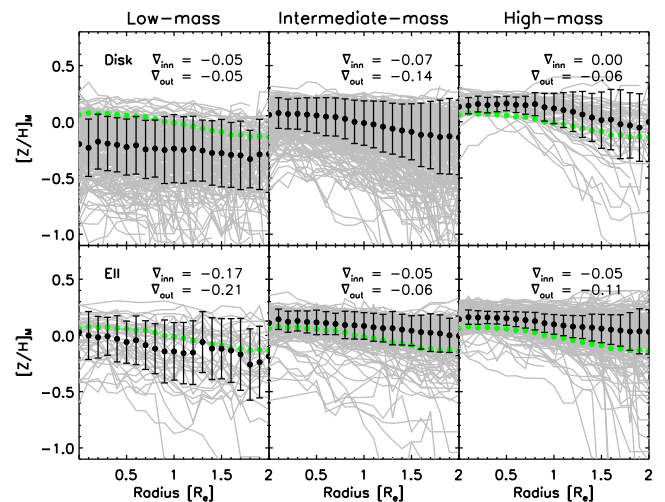

Figure 7. Co-added mass-weighted metallicity profiles. The symbols are the same as in Fig. 4.

Most metallicity profiles have a decreasing trend with increasing radius. For disc galaxies, metallicity decreases more rapidly with increasing radius than that for more massive galaxies. As a result, high-mass disc galaxies have a steeper (more negative) gradient and low-mass disc galaxies have a shallower (close to zero) gradient. Elliptical galaxies are generally more metal rich than disc galaxies, but their gradients look similar at all three mass bins.

Age gradients are usually steeper in the central region ($0 < R < R_e$) than in the outer region ($0.5R_e < R < 1.5R_e$), with the exception that the median luminosity-weighted age profile for low-mass ellipticals has a more positive gradient in the centre than in the outer region. However, metallicity profiles in the central regions are usually shallower than in the outer regions.

We note that the radial profiles of individual galaxies could deviate from the general behaviours described above.

4.2 Dependence on the LSS environment

The LSS environment dependence is the focus of our study. Since stellar mass and colour are known to be correlated with
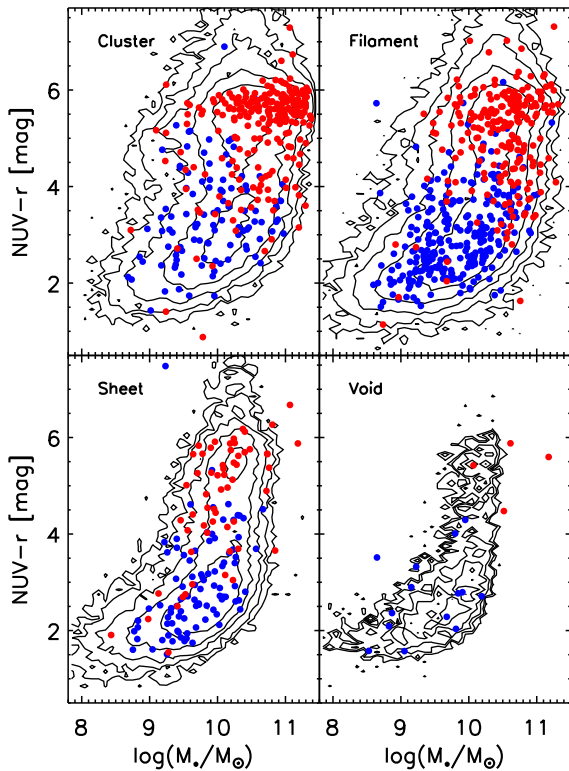
Figure 8. Mass–colour distribution of our sample galaxies in the four LSS environments: cluster (upper left), filament (upper right), sheet (lower right) and void (lower right). Blue dots are for galaxies with Sérsic indices $n < 2.5$ (disc), and red dots are for galaxies with Sérsic indices $n \geq 2.5$ (elliptical). Black contours in the background show the distributions of SDSS DR7 galaxies in the four different LSS environments.

environments (Kauffmann et al. 2004; Blanton & Moustakas 2009), we need to include these parameters in the study. Thus, before showing the LSS environmental dependence, we plot the distributions of two important overall galaxy properties, i.e. stellar mass M_* and $NUV - r$ colour, in different LSS environments (Fig. 8). Note that red galaxies have a much larger portion in denser environments and this is consistent with Lee & Li (2008), Blanton & Moustakas (2009) and Thomas et al. (2010)

In the following two subsections, we explore the LSS environment dependence of both gradients and zero-points, i.e. the fitted values at the effective radius R_e.

4.2.1 Gradients versus LSS environment

We first examine the correlation between the stellar population gradients and the LSS environments. Here, we plot the age and metallicity gradients versus M_*, (Fig. 9) and $NUV - r$ colour (Fig. 10) for different environments. Both age and metallicity gradients are close to zero and slightly negative. They appear to correlate weakly with M_* and $NUV - r$ colour although the correlations changes in different panels of the plots and the scatters are large. The distributions of gradients appear slightly different in different LSS environments, but the difference could be dominated by M_*, although the scatters are large for these plots. We also show gradients of all the galaxies in our sample in the rightmost columns of Figs 9 and 10.

In order to examine the environmental dependence more clearly, we plot the median gradients and the errors of the median values (instead of 1σ scatter) in each mass bin and $NUV - r$ colour bin

in Fig. 11. For low-mass and blue galaxies, there is slight environmental dependence, but differences in different environments are mostly within uncertainties.[4] For high-mass and red galaxies, there are nearly no dependences on LSS environments.

4.2.2 Values at R_e versus LSS environment

An important and also complementary quantity from our line fitting is the fitted age and metallicity values at R_e. These are similar quantities to the central values derived using spectra from single central fibres (e.g. Kauffmann et al. 2004). We plot these values in a similar way to Figs 9 and 10 and the results are shown in Figs 12 and 13. Ages at R_e for both elliptical and disc galaxies are highly correlated with both M_* and $NUV - r$ colour. The metallicity at R_e is also correlated with M_* and $NUV - r$ colour for disc galaxies. For elliptical galaxies, however, $[Z/H](R_e)$ have similar values.

The LSS environment dependence is more obvious in Fig. 14, in which we plot the median values in each mass and colour bin. Low-mass and blue galaxies seem to have some correlations with environment: they have younger ages and lower metallicities in low-density regions. Intermediate-mass and high-mass galaxies do not appear to show this trend. This implies that the LSS environment plays a greater role for smaller galaxies. For massive galaxies, stellar mass plays a dominant role so it matters less where they are located. However, we note that mass-weighted ages of low-mass galaxies and both luminosity and mass-weighted ages of blue galaxies do not show the correlation mentioned above.

4.3 Dependence on local densities

The other important environment indicator is the local density. We calculate the average local mass density within 1 Mpc of each individual galaxy based on the reconstructed density field (Wang et al. 2009, 2014). This is a similar environment indicator to the one used by our companion paper Goddard et al. (2016a) and some previous studies (e.g. Kauffmann et al. 2004).

We present the age and metallicity gradients versus the local density in Fig. 15. Galaxies are colour-coded in M_*, and the mass bins are as defined in Section 4.1. Similar to the LSS environment results, some gradients show a weak trend along different local density environments. For example, low-mass galaxies (top-left panel of Fig. 15) show an increase of luminosity-weighted age gradient towards dense regions; however, the amplitude of variations is comparable to the errors.

We also plot the median values of fitted age and metallicity at the effective radius R_e versus local densities in Fig. 16. The fitted values at R_e show an obvious trend along different local densities. Galaxies have younger ages and lower metallicities in low local density regions. This trend is more obvious for low-mass and blue galaxies and is consistent with the result of previous studies (e.g. Kauffmann et al. 2004; Lin et al. 2014). Again, as in Section 4.2.2, mass-weighted ages of low-mass galaxies and both luminosity and mass-weighted ages of blue galaxies do not show the correlation mentioned above.

---

[4] Note different bins have different number of galaxies and small error bar is usually dominated by large galaxy number in that bin.
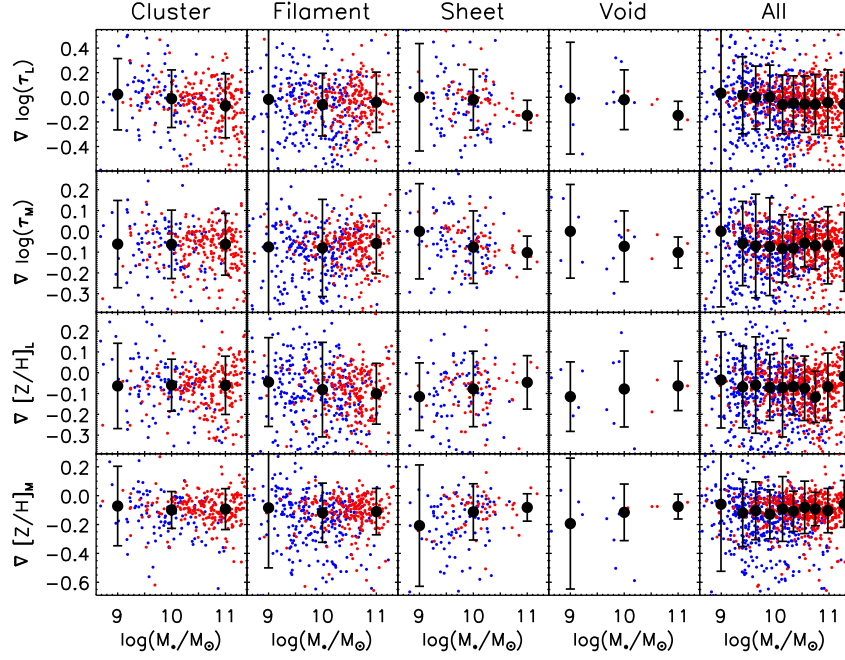
Figure 9. Age and metallicity gradients in units of dex/R_e versus total stellar mass M_* for galaxies in different environments. Red dots are for elliptical galaxies ($n \geq 2.5$) and blue dots are for disc galaxies ($n < 2.5$). The big black dots with error bars show the median value and 1σ scatter of gradients in the three mass bins: $\log(M_*/M_\odot) \leq 9.5$, $9.5 < \log(M_*/M_\odot) \leq 10.5$ and $\log(M_*/M_\odot) > 10.5$. The right-hand column show gradients of all galaxies in our sample using finer mass bins to explore trends with M_*.
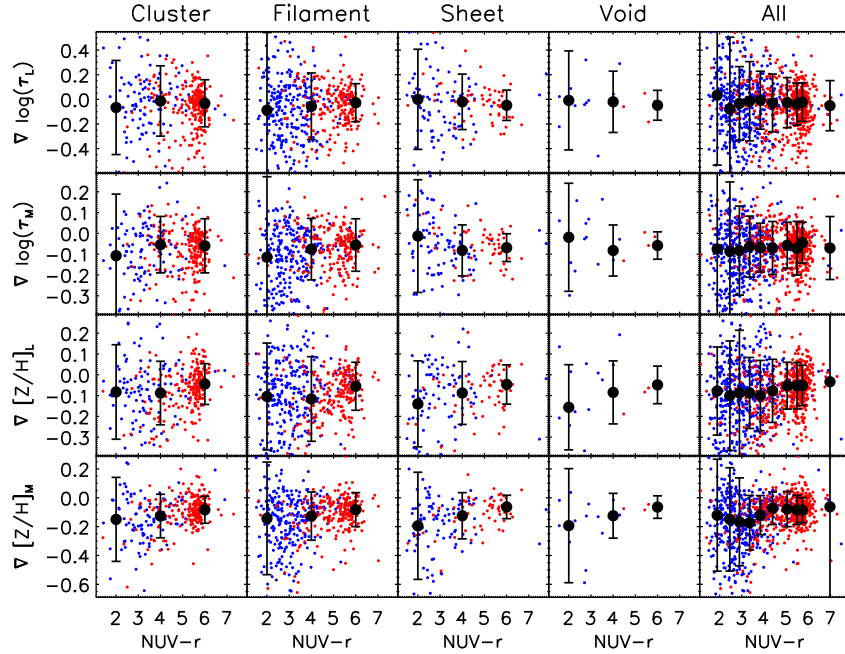
Figure 10. Age and metallicity gradients in units of dex/R_e versus $NUV - r$ for galaxies in different environments. The right-hand column show gradients of all galaxies in our sample. Red dots are for elliptical galaxies ($n \geq 2.5$) and blue dots are for disc galaxies ($n < 2.5$). The big black dots with error bars show the median value and 1σ scatter of gradients in the three colour bins: $NUV - r \leq 3$, $3 < NUV - r \leq 5$ and $NUV - r > 5$. The right-hand column show gradients of all galaxies in our sample and using finer colour bins to explore trends with $NUV - r$ colour.
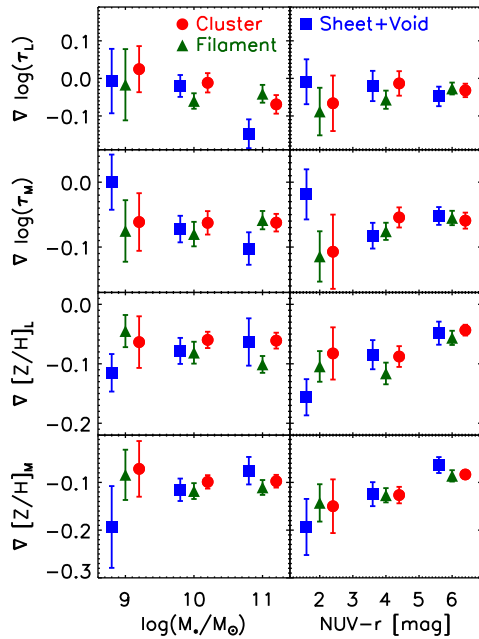
Figure 11. Median gradients and their errors in each mass bin (left-hand panels) and $NUV - r$ bin (right-hand panels). The x-axes are shifted a little bit so that the points do not overlap with each other in the figure. The three mass bins are $\log(M_*/\mathrm{M_\odot}) \leq 9.5$, $9.5 < \log(M_*/\mathrm{M_\odot}) \leq 10.5$ and $\log(M_*/\mathrm{M_\odot}) > 10.5$; and the three $NUV - r$ colour bins are $NUV - r \leq 3$, $3 < NUV - r \leq 5$ and $NUV - r > 5$. Red dots show cluster environment, dark green triangles show filament environment and blue squares show sheet and void environment. A careful reader may have noticed that the error bars in this figure are smaller than those in Figs 9 and 10. This is because the error bars shown here are errors of the median values, which are $1.253\,\sigma/\sqrt{N_g}$, where N_g is the number of galaxies in each mass or colour bin.

5 DISCUSSION

5.1 Comparison with other studies

5.1.1 Gradients

There have been many theoretical predictions for stellar population distributions using different galaxy formation and evolution models. Generally speaking, monolithic collapse models (e.g. Pipino et al. 2010) predict steep metallicity gradients for elliptical galaxies, with a typical slope of about $-0.3\,\mathrm{dex\,dex^{-1}}$. Mergers and stellar migrations would make this gradient much flatter (Roškar et al. 2008; Di Matteo et al. 2009; Sánchez-Blázquez et al. 2009; Minchev et al. 2012).

There have also been many observational studies on age and metallicity gradients for both disc and elliptical galaxies. Almost all of them found slightly negative gradients (Morelli et al. 2015; Roig et al. 2015; González Delgado et al. 2015; Sánchez-Blázquez et al. 2014b), which is consistent with the inside-out galaxy formation scenario. Many previous analyses used a logarithmic definition of gradients, defined as

$$\log(\tau(\log(R/R_e))) = \log(\tau(0)) + k_{\tau,lg} \log(R/R_e), \quad (8)$$

for the stellar age profile, and

$$[Z/H](\log(R/R_e)) = [Z/H](0) + k_{Z,lg} \log(R/R_e). \quad (9)$$

We have also computed gradients using this definition to better compare with previous results. Note that this definition works better for larger radial ranges and gives more weight to the inner regions. We compile the gradients estimated by several recent studies as well as our own results in Table 1. Results calculated using equations (6) and (7) have units of dex/R_e and results calculated using equations (8) and (9) have units of $\mathrm{dex\,dex^{-1}}$.

Rawle et al. (2010) derived stellar population distributions for 25 early-type cluster galaxies using spectral index information. They
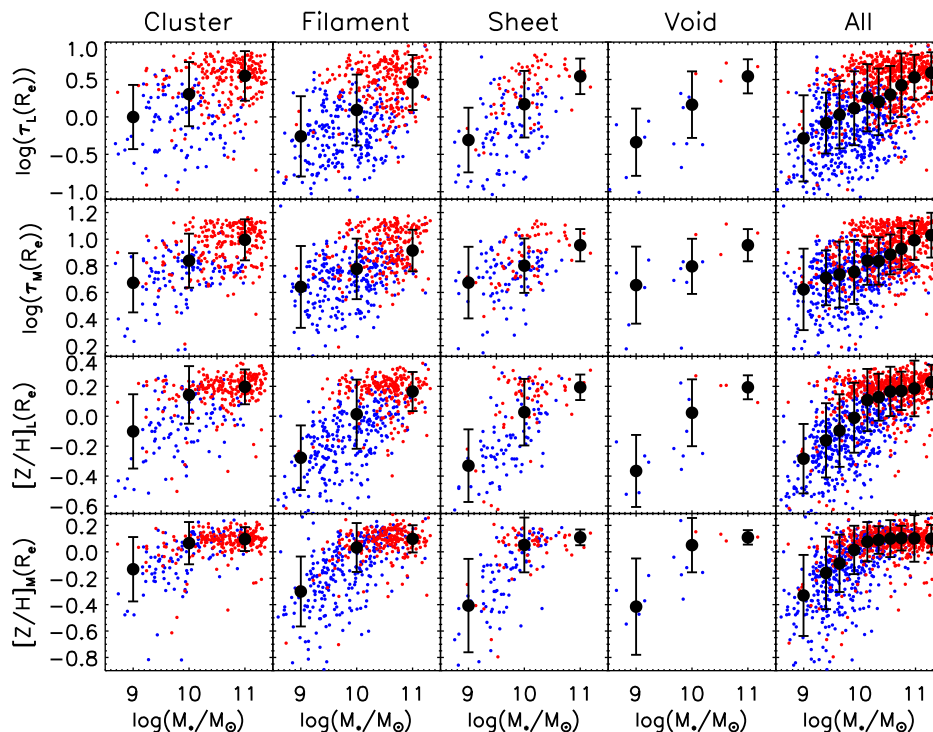
Figure 12. The fitted age and metallicity values at the effective radius R_e. Symbols are the same as Fig. 9.
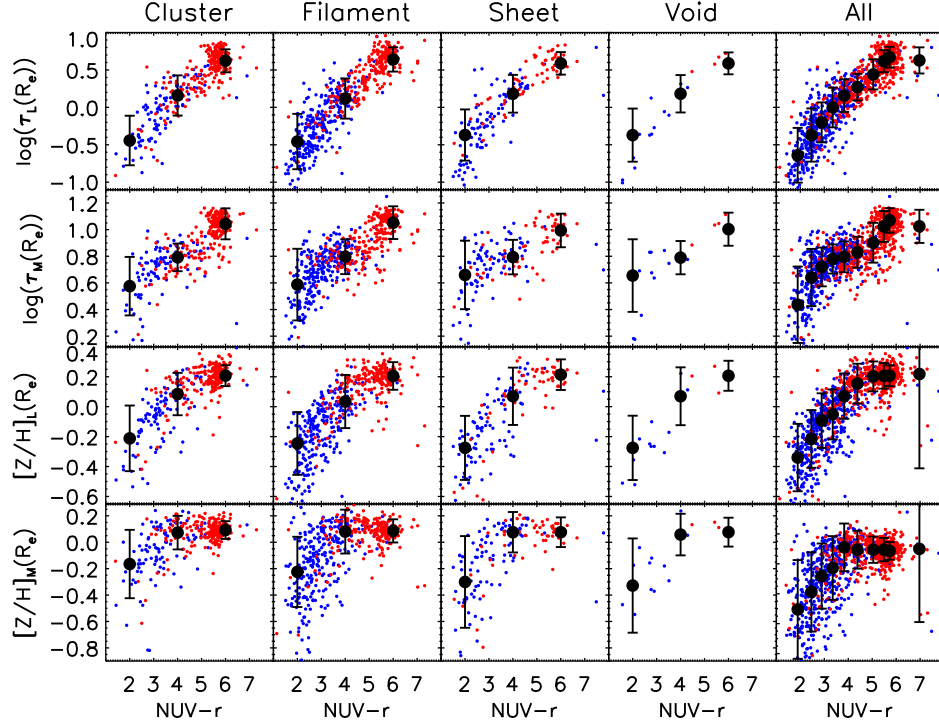
Figure 13. The fitted age and metallicity values at the effective radius R_e. Symbols are the same as Fig. 10.
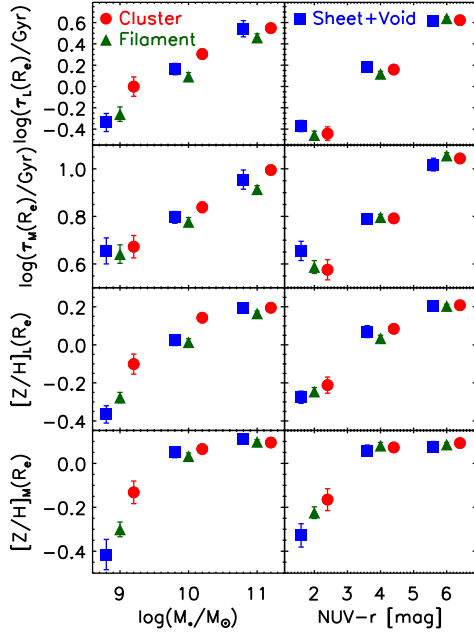

Figure 14. Median values of fitted age and metallicity at the effective radius R_e in each mass (left-hand panels) and $NUV − r$ colour (right-hand panels) bin. Symbols are the same as Fig. 11.
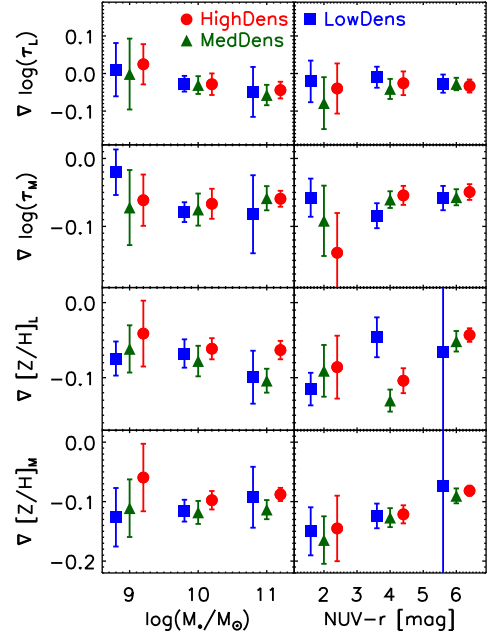
Figure 15. Median gradients and their errors in each mass bin (left-hand panels) and $NUV − r$ bin (right-hand panels). The symbols are now colour-coded in local densities: blue squares show galaxies in low-density ($d_l \leq 2$) regions, green triangles show galaxies in intermediate-density ($2 < d_l \leq 10$) regions and red dots show galaxies in high-density ($d_l > 10$) regions, where the local density, d_l, is the average mass density within 1 Mpc of the target galaxy and is in units of average cosmic mean density, i.e. $7.16 \times 10^{10}\, M_\odot/h/(\mathrm{Mpc}\, h^{-1})^3$ assuming WMAP5 cosmology. The mass-bins and colour-bins are the same as Fig. 11.

found that the mean stellar metallicity gradient for their sample galaxies is $−0.13 \pm 0.04$ dex dex^{-1} and the mean age gradient is $−0.02 \pm 0.06$ dex dex^{-1}. Kuntschner et al. (2010), using a similar spectral index analysis method, studied 48 early-type galaxies from the SAURON[5] sample and found a mean metallicity gradient value

[5] Spectroscopic Areal Unit for Research on Optical Nebulae (Bacon et al. 2001).

Figure 16. Median values of fitted age and metallicity at the effective radius R_e versus local densities. Symbols are the same as Fig. 15.

of -0.25 ± 0.11 dex dex^{-1} for old ellipticals and -0.28 ± 0.12 dex dex^{-1} for young ellipticals, and a mean age gradient value of 0.02 ± 0.13 dex dex^{-1} for old galaxies and 0.28 ± 0.16 dex dex^{-1} for young ellipticals.

Sánchez-Blázquez et al. (2014b), using the full spectral fitting method, studied 62 disc galaxies from the CALIFA[6] sample and found $\nabla[Z/H]_M = 0.000 \pm 0.006$ dex/R_e and $\nabla\tau_M = -0.087 \pm 0.008$ dex/R_e. They further claim that there is no metallicity gradient–M_* correlation.

More recently, González Delgado et al. (2015) studied about 300 CALIFA galaxies with various morphologies and found $\nabla[Z/H]_M = -0.1 \pm 0.15$ dex dex^{-1} for the inner regions (within $1 R_e$) of elliptical and S0 galaxies and a shallower metallicity slope in the 1–3 R_e region. They also found that the metallicity gradients are almost constant for S0 and E (and very massive) galaxies but that there is a weak correlation between metallicity gradient and stellar mass (and morphological types) for disc galaxies. The metallicity gradients become steeper at higher stellar masses with the $\nabla[Z/H]_M$ ranging from -0.4 to 0.4 dex/R_e.

In this paper, we found $\nabla[Z/H]_M = -0.31 \pm 0.04$ dex dex^{-1} (or -0.14 ± 0.02 dex/R_e) for disc galaxies and $\nabla[Z/H]_M = -0.19 \pm 0.03$ dex dex^{-1} (or -0.09 ± 0.01 dex/R_e) for elliptical galaxies. We also found $\nabla\tau_M = -0.18 \pm 0.03$ dex dex^{-1} (or -0.08 ± 0.02 dex/R_e) for disc galaxies and $\nabla\tau_M = -0.13 \pm 0.02$ dex dex^{-1} (or -0.05 ± 0.01 dex/R_e) for elliptical galaxies. Note these mean values and uncertainties are calculated using the MaNGA primary and secondary sample galaxies only because other galaxies do not have a well-defined volume weight. We apply a volume weight correction according to the MaNGA sample selection paper Wake et al. (in preparation). These mean values are consistent with all previous studies.

We found weak or no correlation between the gradients and M_*, which is consistent with Sánchez-Blázquez et al. (2014b) but

---

[6] Calar Alto Legacy Integral Field Area (Sánchez et al. 2012).

slightly different from González Delgado et al. (2015). Our metallicity gradients are shallower than predictions from most of monolithic collapse models by Pipino et al. (2010). Many previous studies (e.g. Tortora et al. 2010; González Delgado et al. 2015) found that colours and metallicity gradients in spiral galaxies are steeper than in elliptical galaxies. Roediger et al. (2011) also found a similar trend using galaxies in the Virgo cluster. We also found age and metallicity gradients are steeper in disc galaxies than in ellipticals, consistent with these studies.

To provide a more direct comparison, we also compute the gradients within 0–1 R_e and plot them versus the total stellar mass on top of CALIFA results (González Delgado et al. 2015) in Fig. 17. The CALIFA results shown here are derived using values at R_e subtracting values at the centre, which is slightly different from our linear fitting. The mass-weighted metallicities (lower panels of Fig. 17) are consistent with each other. The luminosity-weighted age (top panels of Fig. 17), on the other hand, has about 0.2 dex difference. This difference could be due to their different definition of luminosity-weighted age, as their definition tends to put more weight on younger stellar populations (see Section 3.2).

Some previous studies (e.g. Kuntschner et al. 2010; La Barbera et al. 2010; Spolaor et al. 2010; Tortora et al. 2010) have found metallicity gradients for elliptical galaxies have a minimum around $M_* = 10^{10.3} M_\odot$. We also seem to see a minimum median metallicity gradient around this stellar mass in Fig. 9 (row 3, the rightmost column). However, this trend in Fig. 9 is a combination of spirals and ellipticals with gradients derived within 0.5–1.5R_e. In Fig. 17, neither results from CALIFA (González Delgado et al. 2015) nor our results show this trend.

Also, many studies found that younger elliptical galaxies have more negative metallicity gradients and more positive age gradients than older ones (e.g. Hopkins et al. 2009; Sánchez-Blázquez et al. 2009; Rawle et al. 2010; Tortora et al. 2010). Here, we plot the central age versus ages and metallicity gradients for elliptical galaxies from our sample in Fig. 18. The lower-right panel of Fig. 18 shows a weak increasing trend with central age, which is qualitatively consistent with previous results. However, the scatters are large. Other panels do not show this trend.

La Barbera et al. (2005) studied colour gradients of 1700 early-type galaxies in 159 galaxy clusters and found that colour gradients strongly depend on cluster richness. More recently, Tamura et. al. (2000) and Tamura & Ohta (2000, 2003) studied colour gradients of early-type galaxies in clusters and less dense environments and found that the colour gradients do not depend on environment. Tortora et. al. (2011) studied stellar population gradients for a sample of group and cluster galaxies from numerical simulations and found that for low-mass galaxies, age gradients of cluster galaxies are higher (more positive) than those of group galaxies whilst metallicity gradients of cluster galaxies are lower (more negative) than those of group galaxies. The situation is inverted for high-mass galaxies. However, these trends look weak (mostly within 1σ uncertainty), especially for age gradients. Our results show weak or nearly no dependence on both LSS and local density environments and are consistent with Tamura et. al. (2000) and Tamura & Ohta (2000, 2003).

As mentioned in previous sections, we have a one companion MaNGA paper (Goddard et al. 2016a) studying stellar age and metallicity gradients versus galaxy local density environment measured by close neighbours, and another companion MaNGA paper studying stellar population gradients versus galaxy properties (Goddard et al. 2016b). The two companion papers use

Table 1. Comparison with other studies. Note – MW in the Comments column means mass-weighted and r_{d0} in the Radial range column means the radius at which the light starts being dominated by the disc (Sánchez-Blázquez et al. 2014b). The last column shows the references: R10–Rawle et al. (2010); K10–Kuntschner et al. (2010); SB14–Sánchez-Blázquez et al. (2014b); GD15–González Delgado et al. (2015); G–our companion paper (Goddard et al. 2016b). This table is intended to compare our results with a few recent studies, not a complete list of all previous studies. We only use the MaNGA primary and secondary sample galaxies in calculating the mean value and uncertainties listed in this table because other galaxies do not have a well-defined volume weight. We apply volume weight correction according to the MaNGA sample selection paper Wake et al. (in preparation).

Galaxy type	Number	$\nabla \log(\tau)$	∇ [Z/H]	Units	Radial range	Comments	Ref.
Disc	422	-0.08 ± 0.02	-0.14 ± 0.02	dex/R_e	0.5–1.5R_e	MW	This paper
Elliptical	463	-0.05 ± 0.01	-0.09 ± 0.01				
Disc	422	-0.18 ± 0.03	-0.31 ± 0.04	dex dex^{-1}	0.5–1.5R_e	MW	This paper
Elliptical	463	-0.13 ± 0.02	-0.19 ± 0.03				
Early type	25	-0.02 ± 0.06	-0.13 ± 0.04	dex dex^{-1}	0–1.5R_e	Cluster	R10
Early type	48	0.02 ± 0.13	-0.25 ± 0.11	dex dex^{-1}	2 arcsec–1R_e	Old	K10
		0.28 ± 0.16	-0.28 ± 0.12			Young	
Disc	62	0.000 ± 0.006	-0.087 ± 0.008	dex/R_e	r_{d0}–1.5R_e	MW	SB14
All type	300	$-0.4-0.4$	-0.1 ± 0.15	dex/R_e	0–1R_e	MW	GD15
Disc	216	0.07 ± 0.07	-0.102 ± 0.1	dex/R_e	0–1.5R_e	MW	G
Elliptical	505	0.09 ± 0.05	-0.05 ± 0.07				
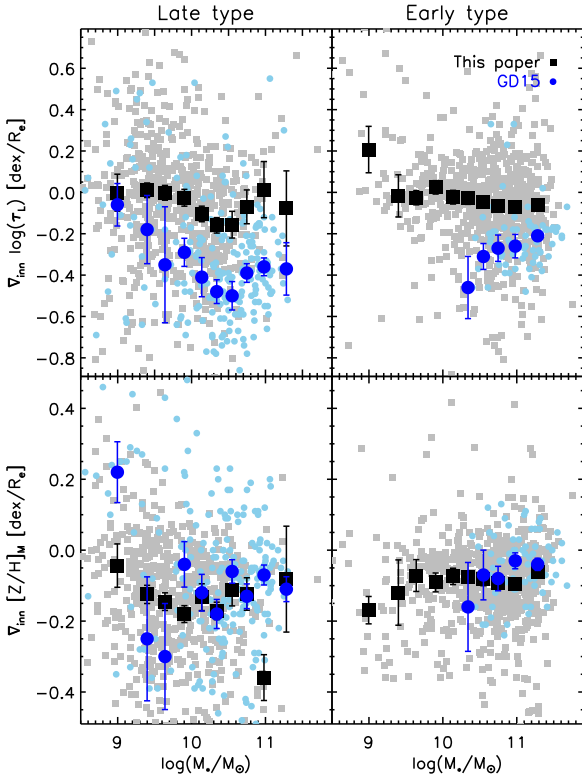
Figure 17. Comparison of inner gradients (between 0 and 1 R_e) between this paper and CALIFA analyses (González Delgado et al. 2015, using GME models). Upper panels show the luminosity-weighted age gradient and lower panels show the mass-weighted metallicity gradient. Left-hand panels show late-type galaxies and right-hand panels show early-type galaxies. Late type is defined as $n < 2.5$ for our galaxies and Hubble type >0 for CALIFA galaxies; and early type is defined as $n \geq 2.5$ for our galaxies and Hubble type ≤ 0 for CALIFA galaxies. Grey squares are our results for individual galaxies, and sky blue points are CALIFA results for individual galaxies. Big black squares and big blue dots with error bars are the median values of each mass bins with standard errors of the median.
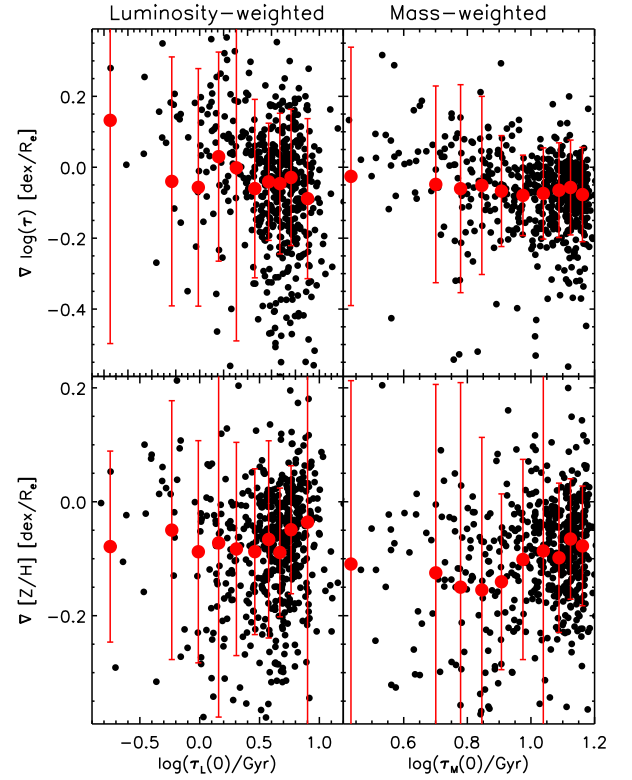
Figure 18. Central ages versus gradients for elliptical galaxies. Left-hand panel show the luminosity-weighted parameters and right-hand panels show the mass-weighted parameters. Black dots show individual galaxies and the big red dots with error bars show median values with 1σ scatter of each central age bin.

different methods from this paper: they use different software (FIRE-FLY; Wilkinson et al. 2015) and different stellar population models (Maraston & Strömbäck 2011) to derive stellar age and metallicity gradients. These differences result in slightly more positive mass-weighted age gradients than ours (see details in Goddard et al. 2016b). Also, they only use the MaNGA Primary sample, which has 721 galaxies and focus on 0–1.5R_e region of each galaxy.

Despite these differences, their results are similar to ours, i.e. stellar age and metallicity gradients do not have an obvious correlation with local density environment (Goddard et al. 2016a).

5.1.2 Values at R_e

There have been many studies about the environmental dependence of overall galactic properties. Although overall galactic properties are different from values at R_e, they should be correlated given that age and metallicity gradients are shallow for most galaxies. For example, Lee & Li (2008) studied overall galactic properties in different LSS environments and found that at fixed luminosity ($9.4 < \log(M_*/M_\odot) < 10$), galaxies in sheet and void environments have lower $D(4000)$ values than those in cluster environments. This implies that galaxies in void and sheet environments have younger luminosity-weighted ages and is consistent with our results shown in Fig. 14. The difference is that we further found that galaxies with smaller stellar masses are more affected by LSS environments. Kauffmann et al. (2004) studied correlations between galaxy properties and local density environments and found that $D_n(4000)$ depends strongly on local density and that the dependence is strongest for low-mass galaxies. This is also consistent with our findings shown in Fig. 16. Mass-weighted ages are more affected by low-mass stars and therefore show smaller differences. Possible mechanisms causing the differences could be harassment (e.g. Moore, Lake & Katzl 1998), strangulation (e.g. Balogh et al. 2000; Peng, Maiolino & Cochrane 2015) or gas stripping (e.g. Gunn & Gott 1972), which could suppress recent star formation in low-mass galaxies in dense environments. We defer further investigation of environmental affects to a future paper, which will use a larger galaxy sample and include halo merger history information from Wang et al. (2016).

5.2 Implications

Fig. 11 shows that age and metallicity gradients have weak or no dependence on LSS. There may be some environmental dependence for low-mass and blue galaxies (e.g. the last row of Fig. 11). The differences in different LSS environments, however, are within a 2σ error. A larger galaxy sample is needed to confirm or disprove this environmental dependence. For high-mass and red galaxies, there are no obvious dependences on LSS environments.

This implies that the galaxy stellar population structure is more affected by previous mergers or by internal processes such as radial migrations. The former could be checked by examining the correlation between stellar population gradients and galaxy merger histories. We are currently determining the merger histories for the dark haloes of all MaNGA galaxies following Wang et al. (2014), as mentioned in Section 3.1, and will present the results in a future paper. The importance of internal process is becoming more and more recognized. In particular, more recent studies (Roškar et al. 2008; Sánchez-Blázquez et al. 2009; Minchev et al. 2012; Zheng et al. 2015) show that stellar radial migration plays an important role in shaping disc galaxies. The co-added metallicity profiles (Figs 6 and 7) show an upturn in the region $>1.5\,R_e$, while the luminosity-weighted age profiles of disc galaxies (upper row of Fig. 4) show a 'U' shape with the minimum located around 1–1.5 R_e. This is similar to the results found by Zheng et al. (2015) using multiband photometric data of 700 disc galaxies (see also Azzollini et al. 2008; Bakos et al. 2008; Radburn-Smith et al. 2012; Yoachim, Roškar & Debattista 2012; Herrmann et al. 2013; Marino

et al. 2016; Ruiz-Lara et al. 2016, etc.), and may be a signature of stellar radial migration as seen in numerical simulations by Roškar et al. (2008). The 'U' shaped age profile is not found in elliptical galaxies (see Figs 4 and 5 and González Delgado et al. 2015). This might be because ellipticals do not have structures such as bars or spiral arms, which are crucial for stellar radial migration models proposed in the literature (Sellwood & Binney 2002). However, there could also be other explanations (e.g. Sánchez-Blázquez et al. 2009; Ruiz-Lara et al. 2016). We have initiated a further project to study the 'U'-shaped age profile using MaNGA data.

6 CONCLUSIONS

We have studied the stellar age and metallicity distributions of 1005 galaxies from the MaNGA MPL-4 internal data release (equivalent to SDSS DR13 public release; Albareti et al. 2016). We have derived the age and metallicities by applying the STARLIGHT package to MaNGA IFU spectra. We have obtained the age and metallicity gradients of each galaxy by fitting a straight line to their age and metallicity profiles over 0.5–1.5R_e, and have explored their correlations with total stellar mass M_*, $NUV - r$ colour and two different environment indicators using the large-scale tidal field and the local density.

We found that the mean age and metallicity gradients are close to zero but slightly negative: mean metallicity gradient $\nabla[Z/H]_M = -0.14 \pm 0.02$ dex/R_e for disc galaxies and $\nabla[Z/H]_M = -0.09 \pm 0.01$ dex/R_e for elliptical galaxies; mean age gradient $\nabla\tau_M = -0.08 \pm 0.02$ dex/R_e for disc galaxies and $\nabla\tau_M = -0.05 \pm 0.01$ dex/R_e for elliptical galaxies. This is consistent with the inside-out formation scenario. The zero but slightly negative gradient is seen as an average over many galaxies; however, gradients for individual galaxies can be positive, negative or zero.

We found that both the age and metallicity gradients have weak or no dependence on either the LSS or the local density environment in the context of our current galaxy sample.

As a complementary investigation, we have also studied correlations between age and metallicity values at the effective radii, and galaxy overall properties as well as environments. Age and metallicity are highly correlated with stellar mass, $NUV - r$ colour and LSS environment and the local density. Low-mass galaxies tend to be younger and have lower metallicity in low-density environments while high-mass galaxies are less affected by environment.

In conclusion, internal processes in galaxy evolution history appear to play a major role in shaping galaxies, especially the high-mass and red galaxies.

REFERENCES

Albareti F. et al., 2016, preprint (arXiv:1608.02013)
Azzolini R., Trujillo I., Beckman J. E., 2008, ApJ, 679, L69
Bacon R. et al., 2001, MNRAS, 326, 23
Bakos J., Trujillo I., Pohlen M., 2008, ApJ, 683, L103
Balogh M., Navarro J. F., Morris S. L., 2000, ApJ, 540, 113
Blanton M., Moustakas J., 2009, ARA&A, 47, 159
Blanton M., Roweis S., 2007, AJ, 133, 734
Blanton M., Eisenstein D., Hogg D. W., Schlegel D. J., Brinkmann J., 2005, ApJ, 629, 143
Blanton M., Kazin E., Muna D., Weaver B. A., Price-Whelan A., 2011, AJ, 142, 31
Bruzual G., Charlot S., 2003, MNRAS, 344, 1000
Bundy K. et al., 2015, ApJ, 798, 7
Cappellari M., Copin Y., 2003, MNRAS, 342, 345
Cappellari M. et al., 2013, MNRAS, 432, 1709
Chabrier G., 2003, PASP, 115, 763
Cid Fernandes R., Mateus A., Sodré L., Stasińska G., Gomes J. M., 2005, MNRAS, 358, 363
Di Matteo P., Pipino A., Lehnert M. D., Combes F., Semelin B., 2009, A&A, 499, 427
Dressler A., 1980, ApJ, 236, 351
Drory N. et al., 2015, AJ, 149, 77
Fitzpatrick P., Graves G., 2015, MNRAS, 1383, 1397
Goddard D. et al., 2016a, MNRAS, preprint (arXiv:1612.01545)
Goddard D. et al., 2016b, MNRAS, preprint (arXiv:1612.01546)
González Delgado R. et al., 2015, A&A, 581, A103
Gunn, J., Gott, J. Richard, 1972, ApJ, 176, 1

Hahn O., Porciani C., Carollo C. M., Dekel A., 2007, MNRAS, 375, 489
Herrmann K., Hunter D. A., Elmegreen B. G., 2013, AJ, 146, 104
Hoffman Y., Metuki O., Yepes G., Gottlöer S., Forero-Romero J. E., Libeskind N. I., Knebe A., 2012, MNRAS, 425, 2049
Hopkins P., Hernquist L., Cox T. J., Keres D., Wuyts S., 2009, ApJ, 691, 1424
Kauffmann G., White S. D. M., Heckman T. M., Ménard B., Brinchmann J., Charlot S., Tremonti C., Brinkmann J., 2004, MNRAS, 353, 713
Kawata D., Gibson B., 2003, MNRAS, 340, 908
Koleva M., de Rijcke S., Prugniel P., Zeilinger W. W., Michielsen D., 2009, MNRAS, 396, 2133
Kroupa P., 2001, MNRAS, 322, 231
Kuntschner H. et al., 2010, MNRAS, 408, 97
La Barbera F., de Carvalho R. R., Gal R. R., Busarello G., Merluzzi P., Capaccioli M., Djorgovski S. G., 2005, ApJ, 626, L19
La Barbera F., De Carvalho R. R., De La Rosa I. G., Gal R. R., Swindle R., Lopes P. A. A., 2010, AJ, 140, 1528
La Barbera F. et al., 2012, MNRAS, 426, 2300
Law D. et al., 2015, AJ, 150, 19
Law D. et al., 2016, AJ, 152, 83
Le Borgne J. et al., 2003, A&A, 402, 433
Lee J., Lee B., 2008, ApJ, 688, 78
Lee J., Li C., 2008, preprint (arXiv:0803.1759)
Li C., Kauffmann G., Jing Y. P., White S. D. M., Börner G., Cheng F. Z., 2006, MNRAS, 368, 21
Lin L. et al., 2014, ApJ, 782, 33
Maraston C., Strömbäck G., 2011, MNRAS, 418, 2785
Marino R. et al., 2016, A&A, 585, 47
Mehlert D. et al., 2003, A&A, 407, 423
Minchev I. et al., 2012, A&A, 548, A126
Moore B., Lake G., Katz N., 1998, ApJ, 495, 139
Morelli L., Corsini E. M., Pizzella A., Dalla Bontà E., Coccato L., Méndez-Abreu J., 2015, MNRAS, 452, 1128
Nair P., Abraham R., 2010, ApJS, 186, 427
Park C., Choi Y.-Y., Vogeley M. S., Gott J. R., III, Blanton M. R., SDSS Collaboration, 2007, ApJ, 658, 898
Pasquali A., Gallazzi A., Fontanot F., van den Bosch F. C., De Lucia G., Mo H. J., Yang X., 2010, MNRAS, 407, 937
Peng Y., Maiolino R., Cochrane R., 2015, Nature, 521, 192
Pipino A., D'Ercole A., Chiappini C., Matteucci F., 2010, MNRAS, 407, 1347
Radburn-Smith D. et al., 2012, ApJ, 753, 138
Rawle T., Smith R. J., Lucey J. R., 2010, MNRAS, 401, 852
Roediger J. C., 2011, Courteau S., McDonald M., MacArthur L. A., MNRAS, 416, 1983
Roig B., Blanton M., Yan R., 2015, ApJ, 808, 26
Roškar R., Debattista V. P., Stinson G. S., Quinn T. R., Kaufmann T., Wadsley J., 2008, ApJ, 675, L65
Ruiz-Lara T. et al., 2016, MNRAS, 456, L35
Schiminovich D. et al., 2007, ApJS, 173, 315
Sellwood J. A., Binney J. J., 2002, MNRAS, 336, 785
Spiniello C., Napolitano N. R., Coccato L., Pota V., Romanowsky A. J., Tortora C., Covone G., Capaccioli M., 2015, MNRAS, 452, 99
Spolaor M., Proctor R. N., Forbes D. A., Couch W. J., 2009, ApJ, 691, L138
Spolaor M., Kobayashi C., Forbes D. A, Couch W. J., Hau G. K. T., 2010, MNRAS, 408, 272
Sánchez S. F. et al., 2012, A&A, 538, A8
Sánchez-Blázquez P. et al., 2006a, MNRAS, 371, 703
Sánchez-Blázquez P., Gorgas J., Cardiel N., González J. J., 2006b, A&A, 457, 809
Sánchez-Blázquez P., Courty S., Gibson B. K., Brook C. B., 2009, MNRAS, 398, 591
Sánchez-Blázquez P., Rosales-Ortega F., Diaz A., Sánchez S. F., 2014a, MNRAS, 437, 1534
Sánchez-Blázquez P. et al., 2014b, A&A, 570, A6
Tamura N., Ohta K., 2000, ApJ, 120, 533
Tamura N., Ohta K., 2003, ApJ, 126, 596

Tamura N., Kobayashi C., Arimoto N., Kodama T., Ohta K., 2000, ApJ, 119, 2134

Thomas D., Maraston C., Schawinski K., Sarzi M., Silk J., 2010, MNRAS, 404, 1775

Tortora C., Napolitano N., 2012, MNRAS, 421, 2478

Tortora C., Napolitano N. R., Cardone V. F., Capaccioli M., Jetzer P., Molinaro R., 2010, MNRAS, 407, 144

Tortora C., 2011 Napolitano N. R., Cardone V. F., Capaccioli M., Jetzer P., Molinaro R.,, MNRAS, 411, 627

van den Bosch F., Aquino D., Yang X., Mo H. J., Pasquali A., McIntosh D. H., Weinmann S. M., Kang X., 2008, MNRAS, 387, 79

Wang H., Mo H. J., Jing Y. P., Guo Y., van den Bosch F. C., Yang X., 2009, MNRAS, 394, 398

Wang H., Mo H. J., Yang X., van den Bosch F. C., 2012, MNRAS, 420, 1809

Wang H., Mo H. J., Yang Xiaohu, Jing Y. P., Lin W. P., 2014, ApJ, 794, 94

Wang H. et al., 2016, ApJ, 831, 164

Wilkinson D. et al., 2015, MNRAS, 449, 328

Yan R. et al., 2016a, AJ, 151, 8

Yan R. et al., 2016b, AJ, 152, 197

Yang X., Mo H. J., van den Bosch F. C., Pasquali A., Li C., Barden M., 2007, ApJ, 671, 153

Yoachim P., Roškar R., Debattista V., 2010, ApJ, 716, L4

Yoachim P., Roškar R., Debattista V., 2012, ApJ, 752, 97

Zheng Z. et al., 2015, ApJ, 800, 120

APPENDIX A: MORPHOLOGY AND CENTRAL/SATELLITE EFFECT

Different morphologies (disc versus elliptical) and different environments within a galaxy group (e.g. central versus satellite) may also affect the age and colour gradients. To test this, we have split our sample into subsamples of disc-like (Sérsic index $n < 2.5$) and elliptical-like ($n \geq 2.5$) galaxies, as well as central and satellite galaxies, and produce plots similar to Figs 11 and 14. Note that some of the results shown here are not robust because the number of galaxies in each bin is small, typically much less than 30.

We present the morphology effect in the left-hand panels of Figs A1 and A2. It can be seen that ellipticals usually have weak gradients (closer to zero). They are also older and more metal rich than disc galaxies. However, the differences between different LSS environments are small and are mostly within the 1σ uncertainty.

Furthermore, we also performed the morphological classification using visual inspection. We visually inspected about 1000 galaxies from the MaNGA MPL-4 sample and classify them as late type (Sa, Sb, Sc, Sd and Im) or early type (E and S0) based on the method described in Nair & Abraham (2010). The results using this classification scheme are presented in the right-hand panels of Figs A1 and A2. For our purpose, it is clear that the two morphological classification schemes (using Sérsic index or visual inspection) lead to very similar results (except for some bins with really small numbers of galaxies).

Sánchez-Blázquez et al. (2006b) studied the central regions of 98 early-type galaxies and found that galaxies in low-density environments appear younger and more metal rich than their counterparts in high-density environments. This appears somewhat different from our results here: we find that low-mass elliptical galaxies in sheet and void regions are both younger and metal poorer than their counterparts in clusters and filaments, and we see no difference for high-mass galaxies between different LSS environments (Fig. A2). It should be noted, however, that the environment and metallicity estimators used here are different from those in Sánchez-Blázquez et al. (2006b). In addition, while they focused on the central parts of galaxies, our results are for regions near R_e.

We also use the central (the most massive galaxy within a galaxy group) and satellite information from the catalogue of Yang et al. (2007) to study the central versus satellite effect. The results are plotted in Figs A3 and A4. Here again, no significant difference
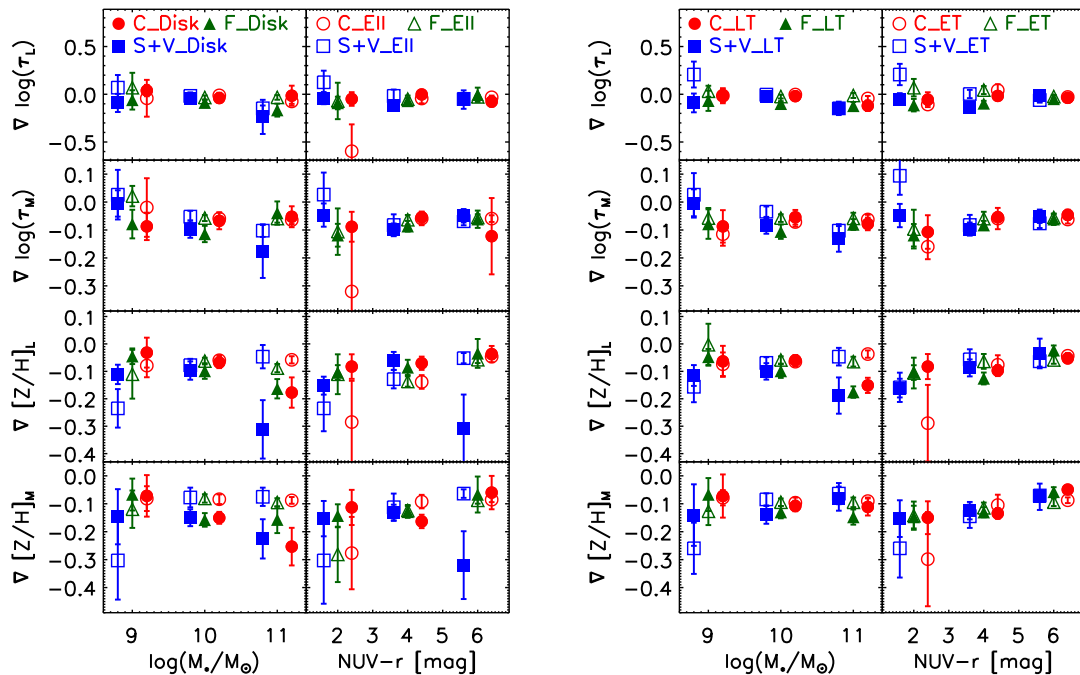

Figure A1. Age and metallicity gradients in each mass and $NUV - r$ colour bin. Red dots show cluster environment (C), green triangles show filament environment (F) and blue squares show sheet and void environment (S+V). Filled symbols show late type/disc galaxies (LT/Disc) and open symbols show early-type/elliptical galaxies (ET/Ell). Left-hand panels show results using morphological classification based on Sérsic index n and right-hand panels show results using morphological classification based on visual classification.
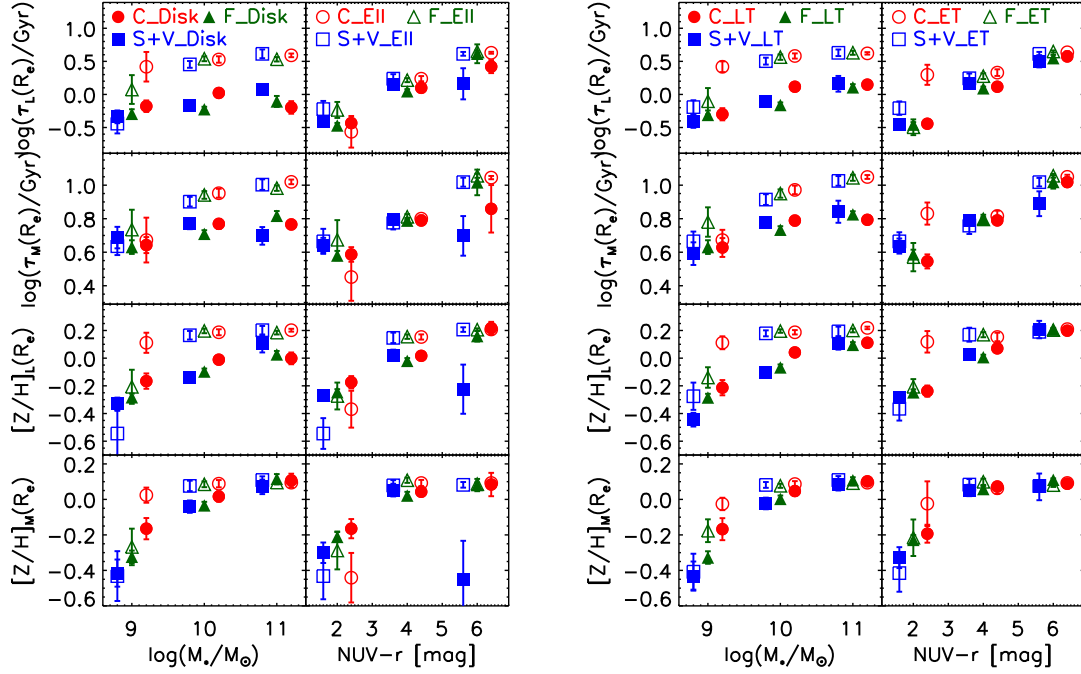
Figure A2. Median values of fitted age and metallicity at the effective radius R_e in each mass and $NUV - r$ colour bin. Panel arrangement and symbols are the same as Fig. A1.
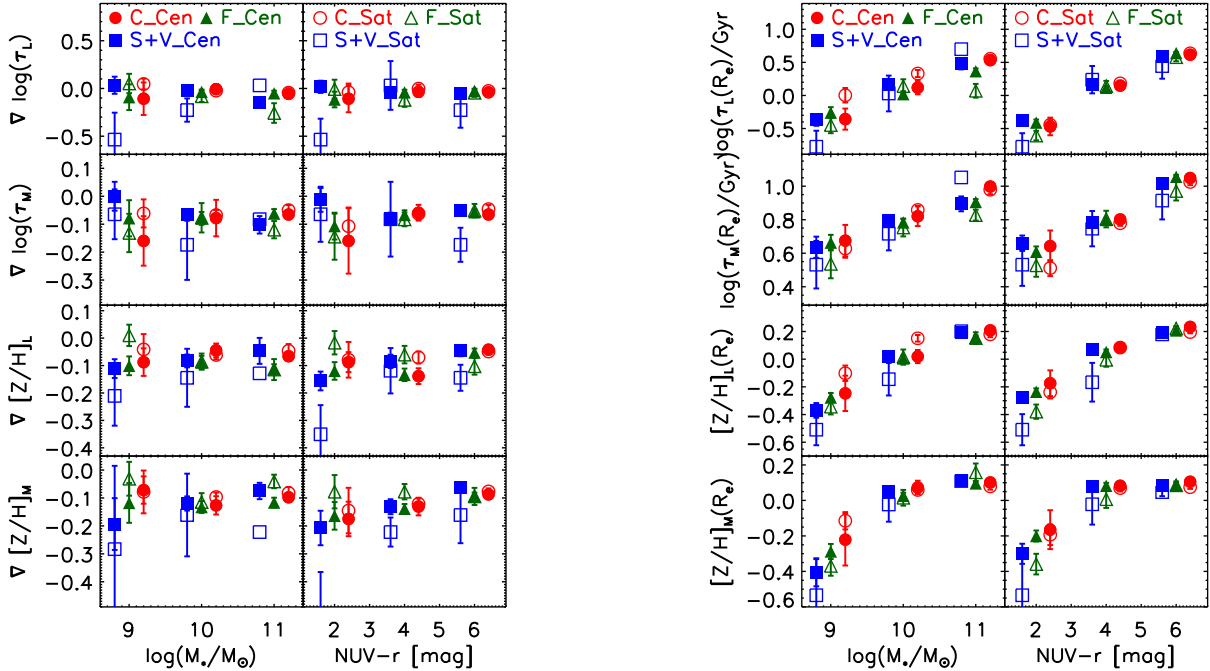

Figure A3. Age and metallicity gradients in each mass (left-hand panels) and $NUV - r$ colour (right-hand panels) bin. Red dots show cluster environment (C), green triangles show filament environment (F) and blue squares show sheet and void environment (S+V). Filled symbols show central galaxies (Cen) and open symbols show satellite galaxies (Sat).

Figure A4. Median values of fitted age and metallicity at the effective radius R_e in each mass (left-hand panels) and $NUV - r$ colour (right-hand panels) bin. Symbols are the same as Fig. A3.

is seen between gradients of centrals and satellites. van den Bosch et al. (2008) studied colour and morphology differences between centrals and satellites and found that satellites are redder than centrals of the same stellar mass. Fitzpatrick & Graves (2015) found that early-type satellites are slightly (0.02 dex) older than early-type
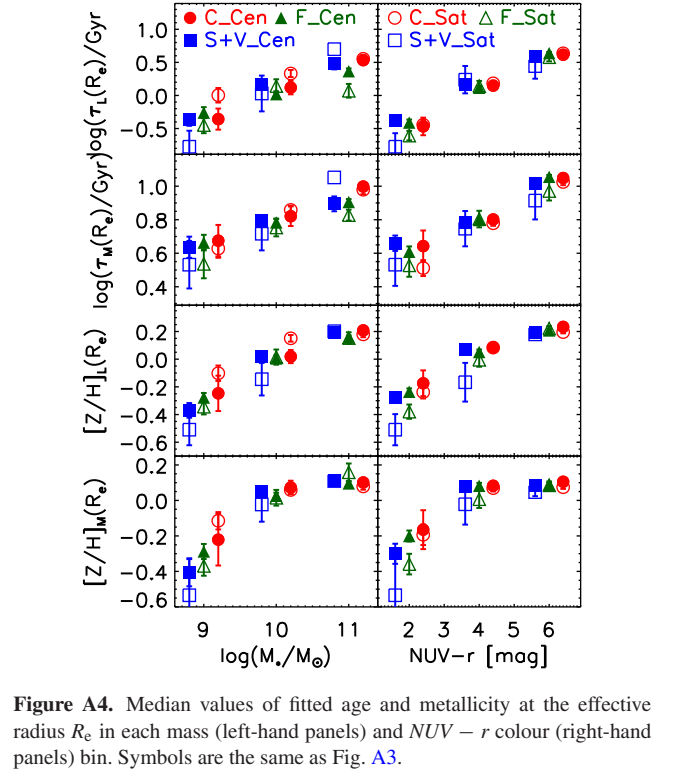
centrals. Pasquali et al. (2010) conducted a more detailed study and found that satellites are older and metal richer than centrals of the same stellar mass, and that this difference increases with decreasing stellar mass. They also found that the differences are less in denser galaxy environments. We observed a similar trend for galaxies in cluster environments (Fig. A4). We found satellite galaxies in sheet and void environments are relatively younger and metal

poorer compared to centrals in the same LSS environments. However, these differences shown in our plots are small by comparison with the error bars.

APPENDIX B: BEAM SMEARING EFFECT

One concern about deriving age and metallicity gradients from MaNGA data is that the gradients might be affected by beam smearing effects. One way to examine the effect of beam smearing is to plot our derived gradients versus angular sizes of the gradient-fitting region (Fig. B1). Ideally, we would expect no correlation between
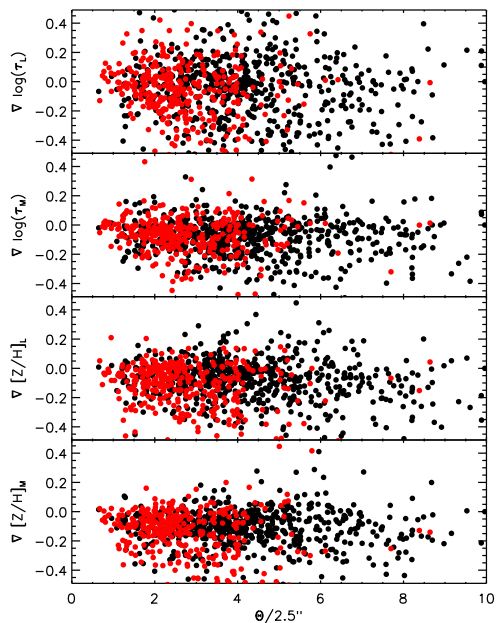

Figure B1. Age and metallicity gradients versus galaxy angular size Θ (=1.5 R_e) in units of beam size (2.5 arcsec). Black dots are for galaxies from the MaNGA primary+colour-enhanced sample and red dots are for galaxies from the secondary sample. This diagram shows that the gradients do not depend on the galaxy angular size.
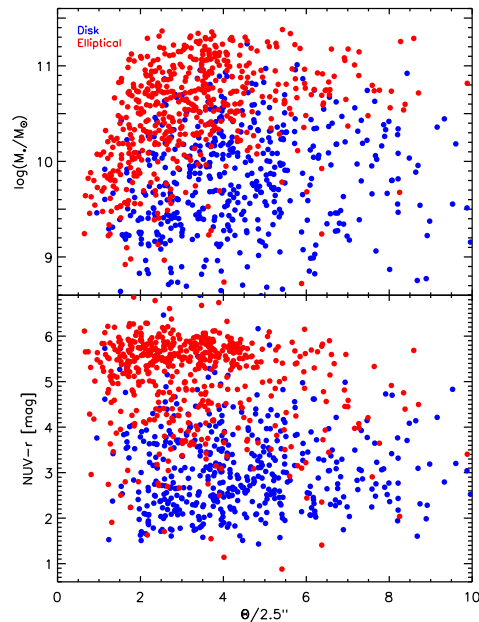

Figure B2. Galaxy overall properties M_* and NUV$-r$ colour versus galaxy angular size Θ in units of beam size (2.5 arcsec). Blue dots are for galaxies with Sérsic indices $n < 2.5$ (disc galaxies), and red dots are for galaxies with Sérsic indices $n \geq 2.5$ (elliptical galaxies).

gradients and angular sizes if any beam smearing effect is small. We can see from Fig. B1 that there is no obvious correlation between gradients and galaxy angular sizes. The weak trend of luminosity-weighted age gradients of MaNGA secondary sample galaxies is dominated by stellar mass. As we can see from Fig. B2, high-mass galaxies tend to have larger angular sizes. Therefore, beam smearing effects should not be a big problem for our purposes.

This paper has been typeset from a TeX/LaTeX file prepared by the author.